# In vivo confinement promotes collective migration of neural crest cells

András Szabó,[1]* Manuela Melchionda,[1]* Giancarlo Nastasi,[2] Mae L. Woods,[1] Salvatore Campo,[2] Roberto Perris,[3] and Roberto Mayor[1]

[1]Department of Cell and Developmental Biology, University College London, London WC1E 6BT, England, UK
[2]Department of Biochemical and Dental Sciences and Morphofunctional Images, School of Medicine, University of Messina, 98122 Messina, Italy
[3]Center for Molecular and Translational Oncology, University of Parma, 43121 Parma, Italy

Collective cell migration is fundamental throughout development and in many diseases. Spatial confinement using micropatterns has been shown to promote collective cell migration in vitro, but its effect in vivo remains unclear. Combining computational and experimental approaches, we show that the in vivo collective migration of neural crest cells (NCCs) depends on such confinement. We demonstrate that confinement may be imposed by the spatiotemporal distribution of a nonpermissive substrate provided by versican, an extracellular matrix molecule previously proposed to have contrasting roles: barrier or promoter of NCC migration. We resolve the controversy by demonstrating that versican works as an inhibitor of NCC migration and also acts as a guiding cue by forming exclusionary boundaries. Our model predicts an optimal number of cells in a given confinement width to allow for directional migration. This optimum coincides with the width of neural crest migratory streams analyzed across different species, proposing an explanation for the highly conserved nature of NCC streams during development.

## Introduction

In vitro studies have shown that cells become more prone to collective migration when they are confined onto micropatterned surfaces (Vedula et al., 2012; Doxzen et al., 2013; Leong et al., 2013; Londono et al., 2014; Marel et al., 2014). To investigate the potential in vivo relevance of this effect, we studied the collective migration of neural crest cells (NCCs), a mesenchymal embryonic cell population whose migratory behavior has been likened to cancer metastasis. NCCs delaminate from the neural tube and migrate large distances in distinct streams as a loosely connected cluster of mesenchymal cells to reach a target area, where they differentiate further. Previous studies of NCC migration identified two essential mechanisms: coattraction (CoA) and contact inhibition of locomotion (CIL; Carmona-Fontaine et al., 2008, 2011; Woods et al., 2014). CoA is the autocrine chemotaxis of NCCs toward the self-secreted and diffusible complement component C3a (Carmona-Fontaine et al., 2011). CIL, on the other hand, is the process whereby colliding cells make contact, repolarize away from one another, and eventually separate. High cell density has been identified previously in epithelial cells as a key requirement for confinement to enhance collective migration (Doxzen et al., 2013; Leong et al., 2013; Londono et al., 2014). However, NCCs exhibit CIL only with other NCCs and not with the surrounding tissues (Carmona-Fontaine et al., 2008, 2011); therefore, they migrate into a region with essentially low cell density. Consequently, the prediction of in vitro studies does not necessarily hold true for NCCs. Despite the detailed studies of CIL and CoA, the role of confinement during in vivo NCC migration has not yet been established.

To experimentally test the hypothesis that NCC migration in vivo is enhanced by spatial confinement, the confining factor needs to be identified. Such a factor is likely to be present in the microenvironment of the NCCs and is expected to restrict migration without affecting cellular motility. Thus the hypothesis predicts a contradictory role for such a factor acting as an inhibitor of migration to form exclusionary boundaries and, at the same time, required for collective migration of NCCs. Studies in amphibian, avian, and mouse embryos have demonstrated a crucial role for extracellular matrix molecules in controlling NCC migration and in particular the chondroitin sulfate proteoglycan versican (Newgreen et al., 1982; Perris and Johansson, 1987, 1990; Perris et al., 1996; Pettway et al., 1996; Kerr and Newgreen, 1997; Perris and Perissinotto, 2000). Studies in mouse and amphibia suggest that versican is expressed in tissues surrounding the neural crest (NC; Casini et al., 2008; Dutt et al., 2011). The role of versican has been controversial, with studies

*A. Szabó and M. Melchionda contributed equally to this paper.

Correspondence to Roberto Mayor: r.mayor@ucl.ac.uk

Abbreviations used in this paper: CIL, contact inhibition of locomotion; CoA, coattraction; CoMo, control morpholino oligonucleotide; CPM, cellular Potts model; DEM, discreet element method; ISH, in situ hybridization; MO, morpholino oligonucleotide; NAM, normal amphibian medium; NC, neural crest; NCC, neural crest cell; PB, phosphate buffer.



The Rockefeller University Press $30.00
J. Cell Biol. Vol. 213 No. 5 543–555
www.jcb.org/cgi/doi/10.1083/jcb.201602083

describing it as either a positive or negative regulator of NCC migration (Landolt et al., 1995; Perissionotto et al., 2000; Dutt et al., 2006, 2011; Casini et al., 2008). Isolated amphibian and avian NCCs are unable to migrate onto a purified versican substrate in vitro (Perris et al., 1991, 1996; Perris and Perissinotto, 2000) and are unable to migrate onto the versican-rich locations in avian and mouse embryos (Perris et al., 1991; Landolt et al., 1995; Henderson et al., 1997; Perris and Perissinotto, 2000; Dutt et al., 2006). Paradoxically, experiments in avian and amphibian embryos indicate that versican acts as a guiding cue for NCC migration (Perris et al., 1990; Stigson et al., 1997; Perissinotto et al., 2000) and, consequently, the precise role of versican remains controversial. One major obstacle in resolving this disagreement is the lack of versican loss-of-function experiments because of the lethality of the versican-null *hdf* (heart defect) mouse mutant, with embryos dying before a possible assessment for NC development (Mjaatvedt et al., 1998; Williams et al., 2005). Nonetheless, these apparently contradictory studies that suggest positive and negative activities of versican on NC migration make versican an ideal candidate molecule for confining NCCs during their movement through the embryo.

Using *Xenopus laevis* embryos, we show that confinement in vivo may be imposed by the spatiotemporal distribution of versican and support our prediction via loss-of-function experiments. We show a quantitative agreement between the effect predicted by computational modeling and our observations in vivo, and we predict an optimal confinement width for a given population size of migrating NCCs that coincides with the width–size relationship of various NC streams in both *Xenopus* and zebrafish.

## Results and discussion

### Versican forms an inhibitory boundary around NC streams

We performed the first comprehensive mapping of versican expression during the early stages of *Xenopus* development and analyzed several of its alternatively spliced variants using a combination of quantitative PCR (qPCR) and Western immunoblotting of all eight currently known isoforms. By using exon-spanning primers for all versican variants, we found that versican V0-1 expression peaks around stage 20 (midneurula; Fig. 1 A, black bar), which coincides with the initiation of NCC migration (Mayor et al., 1995). Although some expression of V3 mRNA is also detected around stage 20, transcription of this isoform continues rising well beyond stage 27, when NCC migration ends (Fig. 1 A, blue bar). All other variants (V0–2, V1a, V1b, V2a, and V2b) remained undetectable, or expressed at very low levels, throughout development (Figs. 1 A and S1 A). Importantly, these observations were confirmed by Western blotting of *Xenopus* whole-embryo lysates, showing that at NC migratory stages V0–1 is the predominant versican form (Fig. 1 B). Based on these findings, we focused on isoform V0-1 throughout this study.

To ascertain whether versican is localized within the tissues surrounding the migrating NC, we analyzed the versican mRNA distribution during NC migration and compared it with the NCC marker *Twist* and the placode markers *Eya1* and *FoxI1C* (David et al., 2001; Pohl et al., 2002). Our results indicate that versican is not expressed by the NCCs themselves but is present in the adjacent tissues, including the placodal ectoderm, pharyngeal mesoderm, and pharyngeal endoderm (Fig. 1, C–G; and Fig. S1, B–D). These findings confirm that versican is present around the NCCs, consistent with previous observations in chicken and mouse embryos (Henderson et al., 1997; Perissinotto et al., 2000), and is not expressed by the migrating cranial NCCs themselves.

Next, to assess whether versican could impede movement of cephalic NCCs, we first cultured NC explants on a dual substrate composed of an area containing only fibronectin and another containing fibronectin together with either BSA (control) or 0.6 µg/ml of purified versican (Fig. 1, H and I). NC explants plated onto the control substrate were able to move across the border between the two areas (Fig. 1 J). However, explants cultured on the dual fibronectin–versican substrate failed to invade the versican-positive region even at versican concentrations as low as 0.3 µg/ml (Fig. 1, K and L). The majority (80%) of the clusters touching the versican border leave the border and return to the fibronectin region, making it unlikely that versican would act as either a haptotactic attractant or a chemoattractant. To test the effect of ectopic versican in vivo, acrylic beads soaked with versican were grafted into the NC migratory pathways and the percentage of embryos exhibiting abnormal NC migration was assessed. In accordance with the in vitro assay, versican-soaked beads inhibited NCC migration locally, whereas control PBS beads did not affect NC migration (Fig. 1, M–Q). These observations corroborate the nonpermissive nature of versican as a migratory substrate both in vitro and in vivo and further show that versican forms a restrictive boundary around the migrating NC.

### Loss of versican in vivo leads to altered NC migration

To experimentally test the hypothesis that removing the confinement would compromise the collective migration of NCCs, we used versican-directed morpholino oligonucleotides (MOs) designed to block splicing or translation of all versican isoforms (as described in Materials and methods), including the isoforms found to be expressed during NCC migration as assayed by qPCR (Fig. 2 A) and Western blot (Figs. 2 B and S2 A). Three different MOs targeting V0–1 were used, and because all of them generated similar phenotypes, we show the result of only one MO, hereafter referred to as VsMO (see Materials and methods). Assessment of NCC migration at stage 21 in embryos that received either injection of a control MO (CoMO) or VsMO revealed that knockdown of versican resulted in a strong inhibition of NCC migration (Fig. 2, C–E). This effect persisted in late migratory stages (27), when a more disorganized distribution of NC was observed (Fig. S2, B–E). In later stages, NC derivatives were affected by VsMO injection, as shown by the reduced number of melanocytes or abnormal cartilage formation (Fig. S2, F–H). It is well established that NC migration requires repulsive and attractive cell interactions, such as CIL and CoA, respectively (Carmona-Fontaine et al., 2008, 2011). Importantly, inhibition of versican with VsMO did not affect CIL and CoA (Fig. S2, I–L). The specificity of the MO was demonstrated by rescue experiments using localized delivery of the versican protein (Fig. S2, N and O).

To demonstrate that versican is required only in tissues surrounding the NC, we performed a series of grafting experiments (Fig. 2, F and G). When NCCs from embryos injected with VsMO were grafted into wild-type embryos, we observed normal NC migration along the three major pathways (Fig. 2 F).

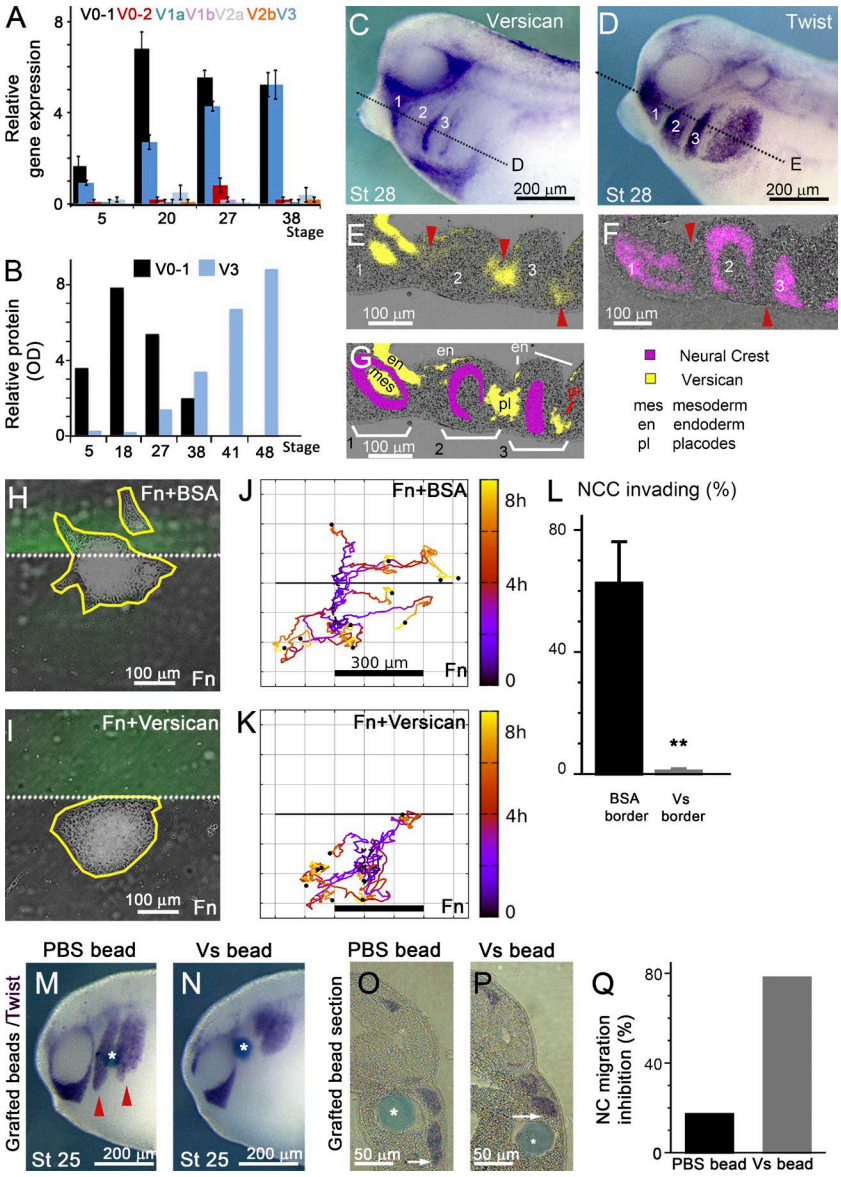


Figure 1. **Versican V0–1 forms a delimiting boundary around migrating NCCs.** (A) qPCR of versican isoforms. Bars, mean; error, SEM. (B) Western blot of V0–1 and V3 isoforms. (C–G) Embryos showing expression of versican (C) and the NC marker Twist (D) using whole-mount in situ hybridization (ISH), and corresponding sections (E and F), with a scheme summarizing the sections (G). Sections on E and F have been enhanced by blurring and squaring the separated ISH signals and overlaid in pseudo-color on the section background. (H–L) NCC explants cultured on fibronectin (Fn) + BSA or Fn + versican barriers invade the barrier area only in absence of versican. (J and K) In vitro cluster trajectories with barrier boundary marked as solid line; $n = 10$; color: time. (L) Percentage of cells invading the barrier ($n = 3$ independent experiments with $n = 251$ and $n = 336$ explants in total for BSA and versican, respectively). Bars, mean; error, SEM. (M–Q) ISH for Twist of embryos grafted with PBS (M) or versican-soaked beads (N), with the corresponding sections (O and P), and inhibition of NC migration (Q; mean inhibition, PBS: $n = 5/29$, versican: $n = 25/32$ embryos). Arrowheads show migrating NCC and asterisks indicate grafted bead. **, $P < 0.01$.

Conversely, when wild-type NC was grafted into VsMO-treated hosts, a clear inhibition of migration was observed (Figs. 2 G and S2 M), indicating that versican is required in the tissues surrounding the NCCs and not in the NCCs themselves for migration to occur. Consequently, our hypothesis suggests that versican forms boundaries between the streams and that its removal of versican might lead to intermingling of NCCs between neighboring streams. To verify whether this was the case, we assessed *Krox-20* expression, as it is known to only be present in alternate streams. Control embryos showed a sharp NC stream emanating from rhombomere 5, whereas in VsMO-injected embryos the streams appeared less advanced, with several cells migrating ectopically into areas of the neighboring stream (Fig. 2, H and I). These observations suggest that versican is required for confinement and that confinement is necessary for efficient collective migration of NCCs.

## Confinement enhances directional collective NCC migration in silico

To test the hypothesis that NCC migration is enhanced by spatial confinement, we apply a computational approach. Although computational models have been previously proposed to explain NC migration, they have not tested the role of spatial confinement (Carmona-Fontaine et al., 2011; Woods et al., 2014; Szabó and Mayor, 2016). One of these models allows cell overlap and arbitrarily high densities (Carmona-Fontaine et al., 2011), which makes it less suitable to explore the effect of confinement. A second model, based on the discreet element method (DEM), overcomes this limitation by representing cells as spheres with a core repulsion defined through contact mechanics (Woods et al., 2014). In this latter model, cell movement is governed by second-order dynamics that allows for frictionless gliding of cell clusters, an assumption that could potentially introduce unexpected modeling artifacts when testing the role of confinement.

To avoid the limitations of these models and to test whether confinement promotes collective migration of NCCs, we present a new model based on the cellular Potts model (CPM) framework (Graner and Glazier, 1992; Fig. 3, A–D). This framework has been widely and successfully applied for studying the effect of confinement on cell migration (Vedula et al., 2012; Doxzen et al., 2013; Londono et al., 2014) but is not specific to epithelia,

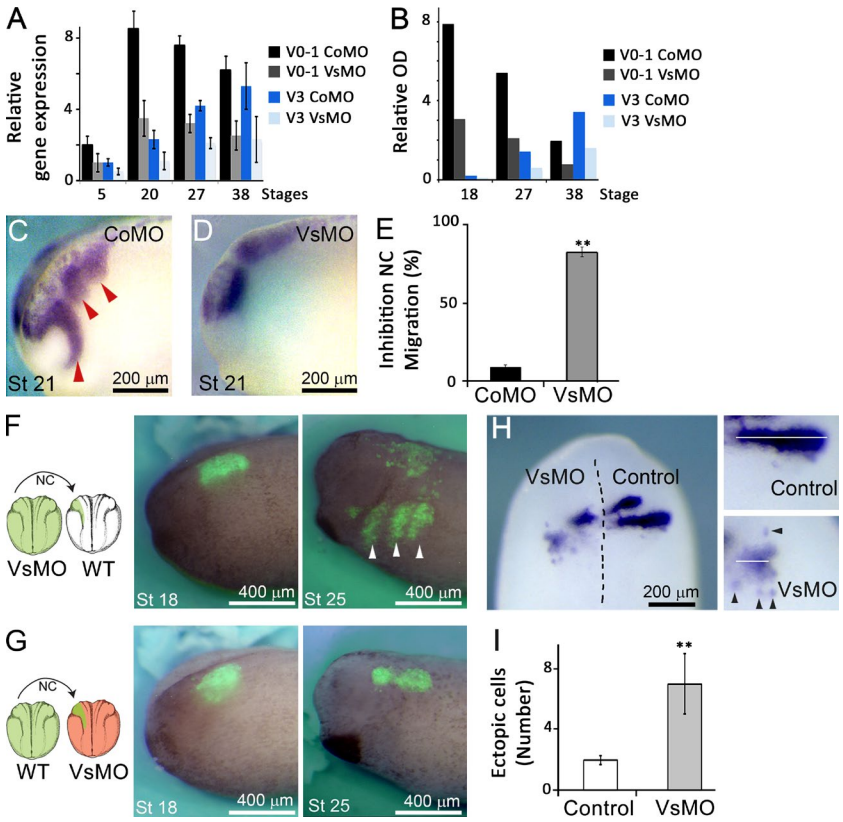


Figure 2. **Versican is required for normal NC migration.** (A and B) qPCR (A) and Western blot (B) analysis of CoMO- and VsMO-injected embryos. (C–E) ISH of Twist in embryos injected with either CoMO (C) or VsMO (D), and inhibition of migration (E; C: $n = 91$, D: $n = 135$). (F and G) Graft experiments: VsMO + fluorescein-dextran (FDx)–injected NCC grafted into control host (F; 76% of migration, $n = 17$) or CoMO + FDx NCC grafted into VsMO-injected host (G; 13% of migration, $n = 15$). (H and I) ISH against Krox20, showing an uninjected versus VsMO-injected side of a stage 24 embryo (H, dorsal view; $n = 53$), and number of ectopic NCC (I; $n = 51$). Bars, mean; error, SEM. Arrowhead represents a migrating NC. **, $P < 0.01$.

as shown by its use in modeling cancer metastasis (Turner and Sherratt, 2002; Rubenstein and Kaufman, 2008; and many others reviewed in Szabó and Merks, 2013), T cell trafficking (Beltman et al., 2007; Vroomans et al., 2012), swarming of bacteria (Jorn et al., 2007), vasculogenesis (Merks et al., 2006; Szabó et al., 2008; Shirinifard et al., 2009), and even dictyostelium movement (Marée et al., 1999). In brief, cells in the model are represented as connected domains on a 2D lattice with a preferential migration direction (polarity) that sets the cell's movement persistence (Szabó et al., 2010). To implement CIL, colliding cells form a cell–cell adhesion contact and they gradually repolarize away from one another to eventually separate (Fig. 3 B). In agreement with previous experimental observations (Theveneau et al., 2010), migratory persistence of cells is increased during contact (Fig. S3 A). This implementation leads to a distribution of contact durations and separation angles (Fig. S3, B and C) similar to those observed experimentally (Woods et al., 2014). To implement CoA, cells secrete a diffusing and decaying chemoattractant, which is sensed by the other cells (Fig. 3 C). CoA acts to prevent dispersion of the cluster in a size-dependent manner (Fig. S3, D and E). In simulations of confinement, lateral restriction is achieved through a localized band of directed force-field acting on the cells, whereas dorsal confinement is implemented by strict exclusion of cells (Fig. 3 D). For more detail on the implementation and parameters, see Materials and methods.

Simulations of the CPM show that a cluster of cells is able to migrate without dispersion and that both CIL and CoA are required for this movement (Fig. 3 E and Video 1). Migration efficiencies, i.e., the percentage of cells migrating ventrally an arbitrary distance of 150 µm within a 3-h period, were calculated from the simulations for the different conditions (Fig. 3 F, black bars). To compare with in vivo migration, equivalent measurements were performed in embryos with fluorescently labeled NC. CoA was inhibited by depleting C3aR (Carmona-Fontaine et al., 2011), whereas CIL was inhibited by expressing Dsh−Dep+, a dominant-negative variant of the PCP signaling pathway (De Calisto et al., 2005; Carmona-Fontaine et al., 2008). Similar migration efficiency was found in most conditions between simulated and in vivo migrating cells (Fig. 3 F, compare black and red bars). Cells without CIL (−CIL+CoA) exhibited similar although slightly higher migration efficiency in vivo than in silico, which could result from the incomplete inhibition of CIL in experiments or from chemotaxis induced by the chemoattractant Sdf1 present in the environment. Clusters of +CIL−CoA cells seemingly migrate efficiently, also supported by the large mean cell displacement over 3 h (Fig. S3 F); however, this movement resembles an enhanced diffusion process (Fig. S3 G; note high dispersion), similar to experimental observations (McLennan et al., 2010; Theveneau et al., 2010; Carmona-Fontaine et al., 2011). These results show that our model based on the CPM is able to reproduce the main aspects of NCC migration, confirming the requirement of CIL and CoA proposed in previous models. Removing lateral confinement in silico results in less directional cluster movement, significantly reduced migration efficiency and mean cell displacements (Fig. 3 G and J, black bars; and Fig. S3 F). This observation is confirmed in simulations using our previously published DEM implementation of NCC migration (Fig. 3, H–J, blue bars; and Video 2). Importantly, this result shows that our prediction is robust, as it does not depend on the particulars of one kind of simulation framework. Together, our results suggest that restrictive boundaries enhance the collective directional movement of NCCs, and when these restrictions are lifted, NC migration is compromised.

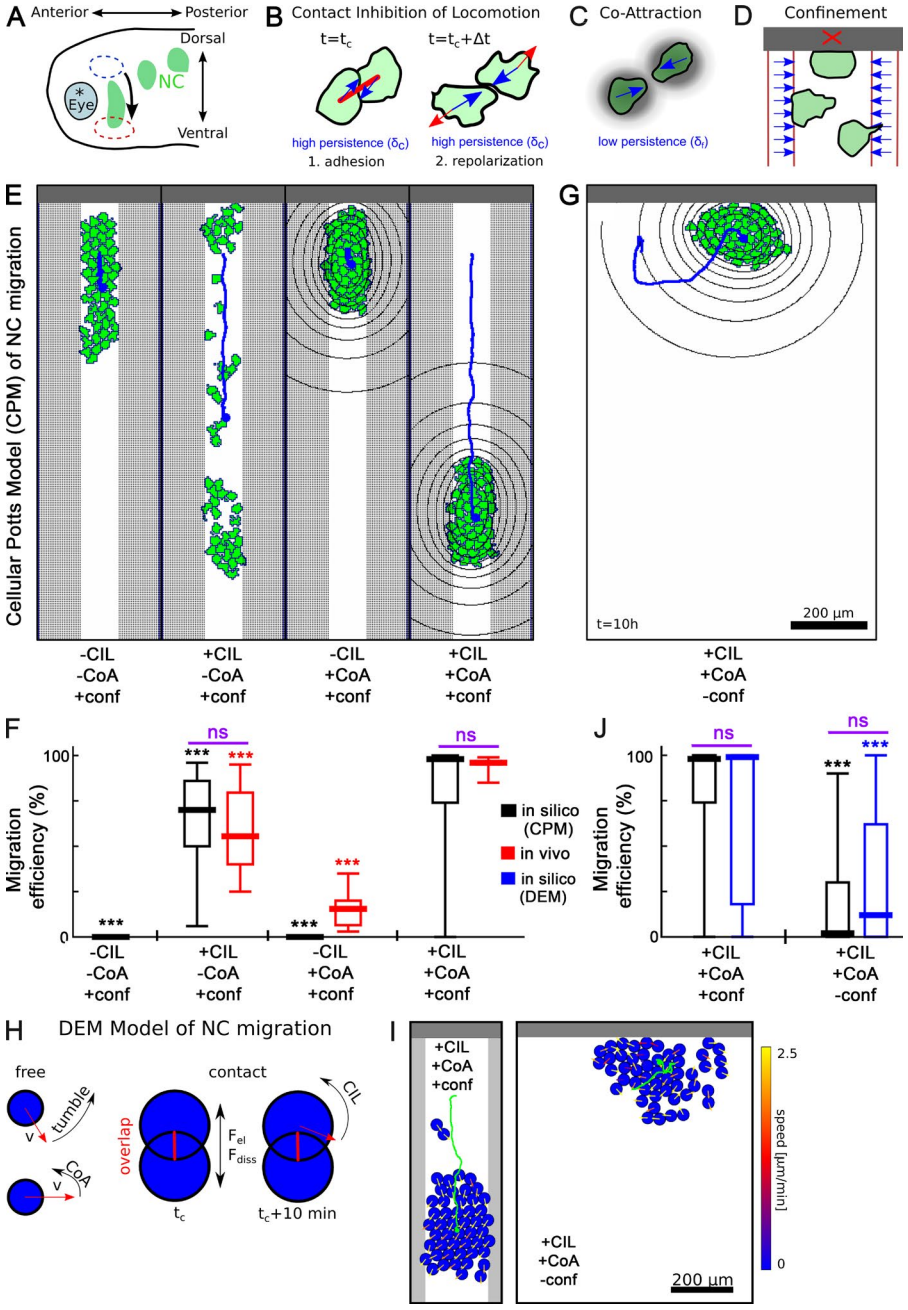


Figure 3. **Computational model of NC migration.** (A) Schematic embryo during NCC migration in the *Xenopus* head. (B–D) Cell interactions in the CPM: CIL (B), CoA (C), and dorsal and lateral confinements (D). (E) CPM configurations for versions of NC migration in constrained geometries with and without CIL and CoA. (F and J) Migration efficiencies. Error bars: min-max values, boxes: quartiles; central value: median; $n = 50$ simulations. Significance compared with relevant control, where significance bars (purple) compare data from the same conditions. (G) CPM configuration in unconstrained geometry. (H) Rules of the DEM model of NCC migration. (I) Configuration of the DEM model with and without confinement. ***, $P < 0.001$; ns, not significant.

Static experimental data are insufficient to confirm this model prediction and a dynamic analysis of NCC movements is required.

### Versican confinement affects movement directionality but not cell motility

To quantify the effect of versican confinement on NCC motility, we analyzed the migratory trajectories of NCCs grafted into CoMO or VsMO-treated host embryos (Fig. 4, A–D; and Video 3) and the trajectories of simulated cells, with or without lateral confinement (Fig. 4, E–H). Importantly, we found that versican depletion in vivo did not affect the ability of cells to move, as shown by the unaltered speed of migrating NCCs (Fig. 4 I), and cell division was also not affected ($3 \pm 0.5 \times 10^{-7}$ divisions per square micrometer per minute in both CoMO- and VsMO-injected embryos). However, persistence of cells is significantly and similarly reduced both in vivo and in silico (Fig. 4 J), which is also reflected in the distribution of the migratory directions (Fig. 4 K). These results show that versican enhances directional migration by confining the NCCs in vivo, and the similarity of the analyzed motility parameters in vivo and in silico provide a quantitative confirmation of our computational model prediction.

To next test whether the observed effect results from the complex environment of the embryo, for example by a self-generated gradient through sequestration of a chemokine as observed during zebrafish lateral line primordial cell migration (Donà et al., 2013), we challenged our model in vitro. We used a previously described "stripe assay" paradigm to mimic in vivo patterns of NCC migration along versican-delineated paths. Accordingly, cultured NC clusters were tracked for 3 h on fibronectin stripes in the presence or absence of versican

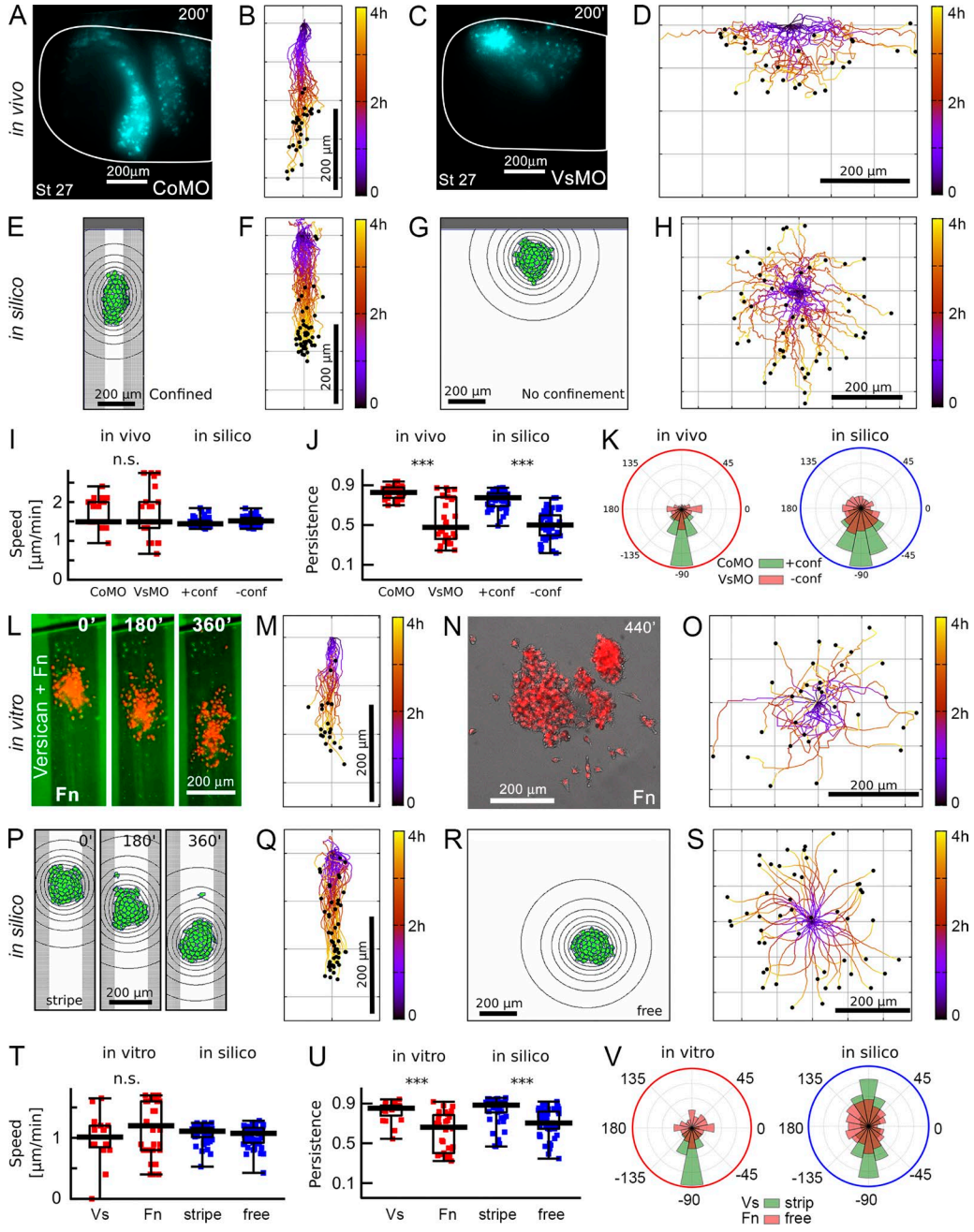


Figure 4. **Confinement by versican enhances collective NC migration.** (A–D) Lateral view of stage 27 embryos of wild-type NC (nuclear-GFP in cyan) transplanted into a CoMO-injected (A, *n* = 21) or VsMO-injected host (C, *n* = 24; Video 3), with cell trajectories (B and D). (E–H) In silico cell migration with and without confinement with cell trajectories (*n* = 50). (I–K) Comparison of cell speed, persistence, and direction of migration in vivo and in silico. (L–O) NC cluster migration in vitro. Frames of time-lapse movie of control NC cluster in versican confinement (L, green: versican, red: NC nuclei; *n* = 20) or without confinement (N; Video 2, *n* = 25) and cluster trajectories (M and O). (P–S) Simulations imitating the in vitro geometries (*n* = 50). (T–V) Comparison of cluster speed, persistence, and direction of migration in vitro and in silico. Error bars, min–max, boxes: quartiles; bar, median. ***, P < 0.001; ns, not significant.

borders (Fig. 4, L–O; and Video 4). In parallel, movement of clusters was simulated in silico with or without confinement as in the stripe assays (Fig. 4, P–S). Absence of confinement did not have major effects on cluster speed but significantly reduced the persistence of clusters in vitro, as determined in silico (Fig. 4, T and U). Confined clusters in silico initiated movement in both directions (dorsal: 23/50, ventral: 27/50; Fig. 4 V; tracks are aligned on Fig. 4, M and Q) and otherwise behaved as the clusters with dorsal confinement. This suggests that the dorsal barrier representing the neural tube in simulations serves only the purpose to determine the initial direction for migration. This is consistent with experimental observations indicating that NCCs grafted into the middle of an already formed NC stream are able to move both ventrally and dorsally (Erickson, 1985). Although several additional factors are expected to influence the NCCs in vivo, our results on cultured NCCs suggest that the confining effect of versican is sufficient to account for the phenotypic change observed by versican loss of function in vivo. We conclude so far that restrictive boundaries are required for the enhancement of NCC migration.

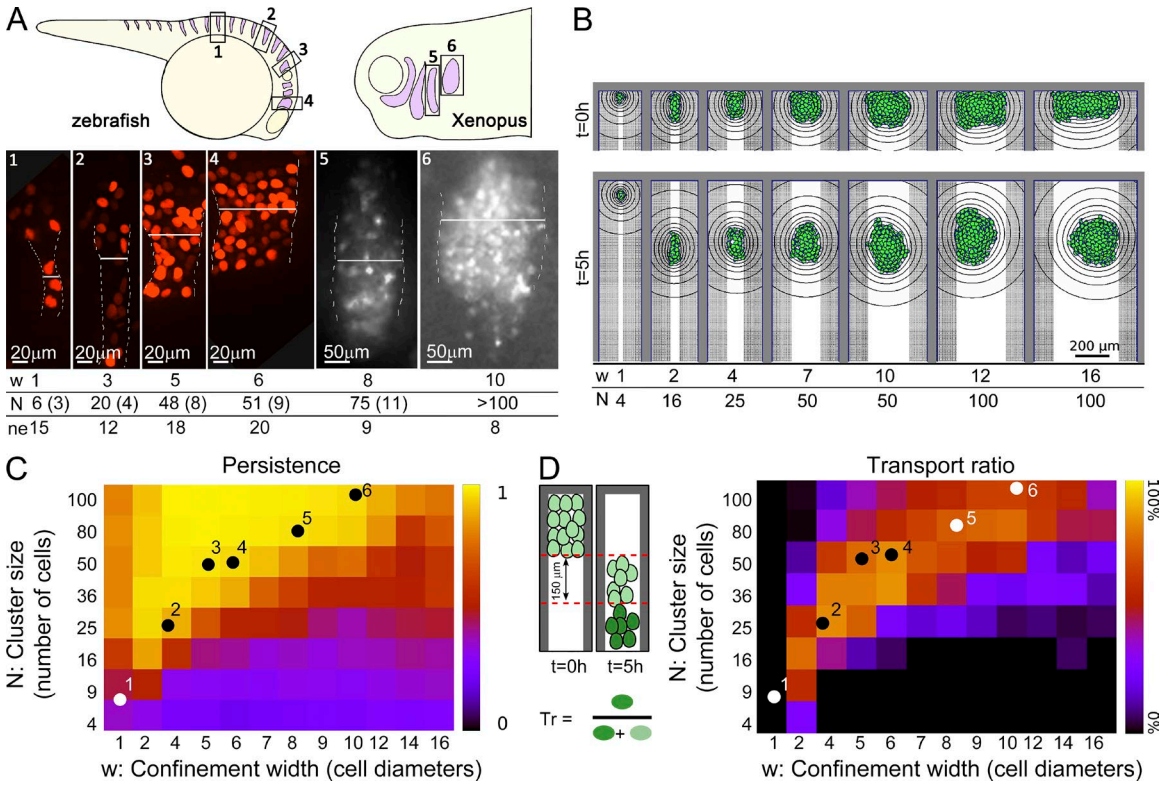


Figure 5. **Effect of confinement width and cluster size.** (A) Schematic illustration and examples of maximal projection of a Z-confocal stack used to measure the number of cells in NC streams of different widths. White line illustrates how the stream width was measured. Width (W) and number of cells (N) are shown at the bottom, with SD in parentheses; ne, number of embryos analyzed. (B) Snapshots of simulations with increasing confinement widths (w, cell diameters) and cluster size (N, number of cells). (C and D) Cluster persistences and transport ratio (percentage of cells in the cluster migrating at least 150 µm away from the cluster's edge in 5 h). Heatmaps represent median values from $n = 50$ simulations. Dots show experimental values for NCs migrating in vivo in zebrafish and *Xenopus* embryos. Numbers on dots correspond to the same numbers shown in A.

### Confinement width and cluster size determine the efficiency of NCC migration

Although migration in streams is conserved across species, a large variability exists in the width of the streams and the number of cells migrating in the stream (size). Width and size are nevertheless stereotypic for each stream. We quantified these in streams along the anterior posterior axis of zebrafish and *Xenopus* embryos using time-lapse imaging and found that streams containing more cells migrate in wider streams (Fig. 5 A).

Next, we used our model to ask whether the width of the confinement influences the migration. We simulated NCC clusters of different sizes ($n = 4$, 9, 16, 25, 36, 50, 80, and 100 cells) in various confinement widths (w = 1-, 2-, 4-, 5-, 6-, 7-, 8-, 9-, 10-, 12-, 14-, and 16-cell diameters; selected configurations shown in Fig. 5 B and Video 5). Clusters migrate persistently in a range of confinement widths, which is determined by the number of cells in the cluster (Fig. 5 C). Importantly, we found that for a given number of cells, persistence increased with the stream width up to a point and decreased in wider streams, indicating an optimal stream width for that cell number. To compare with our in vivo observations, we assume that the stream width observed in vivo is indicative of confinement width. Our measurements show that the confinement width and cluster size in vivo are close to the optimal persistence predicted by the model (Fig. 5 C, dots indicate in vivo data). The small discrepancy between the predicted persistence optimum and the experimental data is likely explained by the fact that confinement also limits the number of NCCs that can be transported in a given time. We quantified the proportion of NCCs in a cluster that enters a target area 150 µm ventral from the initial ventral edge of the cluster in a 5-h time interval (for transport ratio, see Fig. 5 D). We found a remarkable coincidence between the predicted optimum transport ratio and the number of cells in streams of different width (Fig. 5 D, dots indicate in vivo data). This optimum is also consistent with the stream widths and cell numbers in avian embryos as previously published (Kulesa and Fraser, 1998). Furthermore, a reduction in NC migration efficiency was observed in streams where the number of NCCs was reduced by ablation (Kulesa et al., 2000).

Altogether, our model predicts an optimal confinement width for a given cluster size. This suggests that during evolution, the number of migrating NCCs have been optimized depending on the stream width, and it is tempting to speculate that this mechanism is conserved across species.

Overall, our results show that the width of confinement within the embryo is not independent of the size of the migrating cluster. How this coordination is established remains to be uncovered. One possibility is genetic hard-wiring, whereby confinement width and the number of differentiating NCCs are genetically encoded in the developmental program of embryos. Another possible explanation is a dynamic emergence of confinement based on local cell interactions, such as the "chase and run" phenomenon, whereby the NCCs move by chemotaxis toward the surrounding cells that express the confinement molecules, and these cells actively move away from the NCCs upon contact (Theveneau et al., 2013). The chase and run mechanism

has been demonstrated to operate between NC and placodal cells and, as demonstrated here, placodes express versican, suggesting that this interaction could lead to a dynamic establishment of confinement. When NCC migration is impaired by VsMO, placodes remain disorganized (Fig. S2 P), similar to what has been shown in the case of NC ablation (Theveneau et al., 2013). The dramatic effect caused by knocking down only a single inhibitory molecule suggests that versican may also play a direct or indirect role in the organization of cells expressing any other repellent molecules adjacent to the NC, such as Ephrin/Eph receptor, Slit/Robo, or semaphorin (Kawasaki et al., 2002; Baker and Antin, 2003; De Bellard et al., 2003; Jia et al., 2005; Mellott and Burke, 2008; Roffers-Agarwal and Gammill, 2009; Schwarz et al., 2009; Theveneau and Mayor, 2012).

In conclusion, our data demonstrate for the first time the relevance of geometrical confinement on collective cell migration in vivo and identify a candidate molecular mechanism for this phenomenon during embryogenesis. Indeed, we provide evidence that migration of the NC depends on such confinement, and we identify the confining molecule, versican, that acts as a nonpermissive substrate for the NCCs. Our results shed light on a new fundamental mechanism governing NCC migration and contribute to a better understanding of the evolutionarily conserved nature of stream formation during NC migration.

## Materials and methods

### RNA isolation, cDNA synthesis, and qPCR amplification

Total RNA was isolated from wild-type and versican-knockdown *Xenopus* embryos at different stages of development (stages 5, 18, 27, and 38) for real-time reverse-PCR analysis of versican variants V0–1, V0–2, V1a, V1b, V1c, V2a, V2b, and V3 by using the Omnizol Reagent kit (Euroclone). The first strand of cDNA was synthesized from 1.0 µg total RNA using a high-capacity cDNA Archive kit (Applied Biosystems). β-Actin mRNA was used as an endogenous control to allow the relative quantification of versican and its splicing isoforms. Primers and probes for real-time PCR were designed and supplied by Applied Biosystems. All probes were labeled with 5′-FAM reporter dye and 3′Black Hole Quencher1 (Table 1). Real-time PCR reactions were performed in triplicate and in monoplex on the model 7500 RT-PCR real-time system (Applied Biosystems) using the TaqMan Universal PCR Mastermix kit (Applied Biosystems) as suggested by the manufacturer. The amplified PCR products were quantified by measuring the calculated cycle thresholds of V0–1, V0–2, V1a, V1b, V1c, V2a, V2b, V3, and β-actin mRNA. The amounts of specific mRNA in samples were calculated by the DDCT (Delta-Delta-Ct) method. The values of the V0–1 gene expression level of the versican wild-type and knockdown embryos at stage 5 were used as a calibrator, and results are expressed as the n-fold difference relative to these values (relative expression levels).

Table 1. **Primer and probe sequences**

| Target | Primer and probe sequences |
|---|---|
| Versican V0-1 | Forward: 5′-ACCATACCAACATTGCCACC-3′ |
| | Reverse: 5′-TGATACTTCCACTTTGGGCC-3′ |
| | Probe: 5′-6FAM-CCACAGTTTTGGTGCC-3′BHQ1 |
| Versican V0-2 | Forward: 5′-GCTAGTTGATGGATGTCCAAC-3′ |
| | Reverse: 5′-AGGAACTTGTCGAATGAGAC-3′ |
| | Probe: 5′-6FAM-CTTCCCCGCCGACTTC-3′BHQ1 |
| Versican V1a | Forward: 5′-GTCATTGCCATGTACTACC-3′ |
| | Reverse: 5′-TTTGGATCAGTGGAGTTTAGC-3′ |
| | Probe: 5′-6FAM-ACTTCACTGCGGAGGTC-3′BHQ1 |
| Versican V1b | Forward: 5′-AGATCGATGTGGGTGAAATC-3′ |
| | Reverse: 5′-TGAGAAGTGTCTTTGAGTCC-3′ |
| | Probe: 5′-6FAM-CAGGCTTTGTCCAGGC-3′BHQ1 |
| Versican V1c | Forward: 5′-GGAATTTCGCAACCATAGCG-3′ |
| | Reverse: 5′-CCCAAAGCCAAATTACGTGC-3′ |
| | Probe: 5′-6FAM-GACGGTCAATATCCATCC-3′BHQ1 |
| Versican V2a | Forward: 5′-GGTGAATTCCGTTGAATCCG-3′ |
| | Reverse: 5′-ATTCCGGCCGTTACGCATAA-3′ |
| | Probe: 5′-6FAM-CACGATCCCTGCATTC-3′BHQ1 |
| Versican V2b | Forward: 5′-TTGGCTAGGGAATACGGGAT-3′ |
| | Reverse: 5′-CCCGAATTCATACCGTGAATT-3′ |
| | Probe: 5′-6FAM-GAACACTGGGATAGCG-3′BHQ1 |
| Versican V3 | Forward: 5′-TTAAGAAGAGGGCACCTTGG-3′ |
| | Reverse: 5′-AGGAGTGGACAGTTTCCCAA-3′ |
| | Probe: 5′-6FAM-GCACAGTAATGCTGCG-3′BHQ1 |
| β-Actin | Forward: 5′-GCTTCTCTTCCAGCCATCG-3′ |
| | Reverse: 5′-GACAGCACAGTGTTGGCATA-3′ |
| | Probe: 5′-6FAM-TCGGTATGGAGTCCTGC-3′BHQ1 |

BHQ1, Black Hole Quencher1.

### Western blotting

For SDS-PAGE and Western blotting, wild-type and versican-knockdown embryos at different stages of development (considered stages: 5, 18, 27, 38, 41, and 45) were washed twice in ice-cold PBS and subsequently dissolved in SDS sample buffer (62.5 mM Tris-HCl, pH 6.8, 2% wt/vol SDS, 10% glycerol, 50 mM DTT, and 0.01% wt/vol bromophenol blue). Aliquots of whole-cell protein extract (10–25 µl/well) were separated by gradient 3–10% gel electrophoresis. The proteins were blotted onto polyvinylidene difluoride membranes (GE Healthcare) using a semidry apparatus (Bio-Rad Laboratories). The membranes were then incubated overnight in a roller bottle with the specific diluted (1:1,000) primary antibody that recognizes all versican isoforms in 5% BSA, 1× PBS, and 0.1% Tween-20 at 4°C. After being washed in three stages in wash buffer (1× PBS and 0.1% Tween-20), the blots were incubated with the diluted (1:2,500) secondary polyclonal antibody (goat antirabbit conjugated with peroxidase), in TBS/Tween-20 buffer, containing 5% nonfat dried milk. After 45 min of gentle shaking, the blots were washed five times in wash buffer, stained with DAB liquid substrate (Sigma-Aldrich), and subjected to densitometric analyses.

### Morpholino oligo

One translational MO, coded VsATGMO (Gene Tools, Inc.) was designed based on the sequence of *Xenopus* versican around the 5′ end of the gene. The sequence of VsATGMO used was 5′-TCTTGACCT TTTAAGGTGACCTAGT-3′. In addition, two splicing MOs, coded VsMO1 and VsMO2 (Gene Tools, Inc.), were designed based upon the sequence of the G3 domain at the carboxyl terminus of the *Xenopus* versican. The sequences of the MOs used were VsMO1 5′-AAG TAAATTTGGATCTTACCTTGCA-3′; VsMO2 5′-GGGTCTTGA CCTGAAATAAGACATT-3′. A similar phenotype was achieved with all MOs when 30 ng and 100 ng of the VsMO1/2 and VsATGMO were injected per embryo, respectively. As all the MOs produced a similar phenotype, we mainly used VsMO2. A standard CoMO with sequence 5′-CCTCTTACCTCAGTTACAATTTATA-3′ was used. Injection of 30 ng of this CoMO into wild-type *Xenopus* embryos had no effect. All oligos were dissolved to 8 µg/µl in nuclease-free water and stored at RT. The efficiency of the morpholinos to inhibit splicing was analyzed by performing real-time qPCR and Western blotting analyses. The specificity of the VsMOs was ascertained by rescuing experiments using localized versican protein. In brief, beads

soaked with versican protein were grafted next to the prospective streams in embryos previously injected with VsMO, followed by analysis of NC migration.

### Embryo manipulation and whole-mount in situ hybridization

*Xenopus* females were stimulated by hCG injections (1,000 U), and embryos were in vitro fertilized using sperm macerated in 1× MMR (100 mM NaCl, 2 mM KCl, 1 mM $MgSO_4$, 2 mM $CaCl_2$, 5 mM Hepes, and 100 µM disodium-EDTA, pH 7.6). Embryos were dejellied in 2% L-cysteine solution to remove the jelly. Embryos were injected and left to recover overnight in normal amphibian medium (NAM) 3/8 with 3% Ficoll. Embryos were transferred and maintained in NAM 1/10 (Beck and Slack, 1999). Embryos were staged according to Nieuwkoop and Faber (1967). Whole-mount in situ hybridization analysis was performed as described previously (Harland, 1991). The following probes were used: *Eya1* (David et al., 2001), *Foxl1C* (Pohl et al., 2002), *Slug* (Mayor et al., 1995), *Twist* (Hopwood et al., 1989), and *Versican* (Casini et al., 2008).

### Preparation of embryos for cryosectioning

Wild-type or experimental embryos were fixed for 2 h in MEMFA at RT and rinsed three times with 1× PBS. Embryos were then washed two times for 5 min in 0.1 M phosphate buffer (PB; 0.2 M $NaH_2PO_4$*$H_2O$ and 0.2 M $K_2HPO_4$, pH 7.4) and incubated overnight at 4°C in 15% sucrose (Sigma-Aldrich) in 1× PB. A solution of 7.5% of type A gelatin from porcine skin (G9136; Sigma-Aldrich) and 15% sucrose in 1× PB was prepared by dissolving at 42°C until the solution became transparent. The embryos were incubated in the gelatin solution at 42°C for at least 45 min. The bottom of a weighing boat was coated with a layer of gelatin and allowed to set. The samples were placed on the gelatin layer and the mold was filled with gelatin solution to entirely cover the samples. The embryos were oriented and blocks were cut to size under an MZ6 dissecting stereomicroscope (Leica Biosystems). The blocks containing the embryos were snap frozen using isopentane prechilled at −80°C. The samples were sectioned using a CM-3050S cryostat (Leica Biosystems) to yield longitudinal sections of thickness between 30 to 40 µm. Sections were placed onto slides (VWR International) and air-dried overnight at RT. The gelatin was removed by incubating the slides in a water bath at 37°C in 1× PBS for 30 min. All sections were mounted on slides with MoWiol (EMD Millipore).

Sections of in situ hybridization (ISH) presented in Fig. 1 (D and E) and Fig. S1 (D and E) have been inverted and split to separate color channels. The green channel containing most of the ISH signal was contrast enhanced to remove any nonspecific background, blurred (ImageJ, Gaussian blur, 3-pixel radius), squared pixel by pixel (ImageJ, Image Calculator). The processed image was merged in pseudocolor with the blue channel of the inverted ISH image containing only background. The final image was contrast enhanced.

### Preparation of NCC cultures

The cephalic NCCs were explanted from stage 18/19 *Xenopus* embryos as previously described (Alfandari et al., 2003; DeSimone et al., 2005). In brief, using an eyebrow knife, the anterior epidermal layer near the neural tube was removed, exposing the NC tissue. The eyebrow knife was then used to gently detach the NC cluster from the surrounding tissues. Once isolated, the NC explant was transferred to a dish containing 1× Danilchick's solution (53 mM NaCl, 5 mM $Na_2CO_3$, 4.5 mM K-gluconate, 32 mM sodium-gluconate, 1 mM $MgSO_4$, 1 mM $CaCl_2$, 0.1% BSA, and 50 µg/ml streptomycin, pH 8.3) and divided into smaller clusters of NC cells, before transferring them to a Petri dish coated with fibronectin (Fn; Sigma-Aldrich).

### In vivo bead grafting and NC transplantation assays

Affigel blue agarose beads (100–200 mesh; Bio-Rad Laboratories) were thoroughly washed in 1× PBS and incubated overnight at 4°C with either PBS or the versican V0/V1 protein. Versican V0/V1 protein was used at a concentration of 11 µg/ml. Embryos were demembraned and allowed to heal for 30 min in NAM 3/8. One single bead was grafted at stage 20 into the preplacodal field near the premigratory NC tissue. The embryos were allowed to heal for 30 min at RT before placing them at 14.5°C until they reached stage 28.

Wild-type, CoMO, or VsMO-injected NC, labeled with fluorescein-dextran (Invitrogen) were explanted as outlined in Preparation of NCC cultures and transplanted into control or VsMO-injected host embryos immobilized in plasticine. The NC explant was held in place with a small glass coverslip for 45 min at RT until the embryos had healed. Once healed the embryos were kept in NAM 3/8 at 14.5°C until they reached stage 28. Experimental embryos from both assays were fixed in 1× MEMFA (4% formaldehyde, 0.1 M MOPS, 1 mM $MgSO_4$, and 2 mM EGTA) for 1 h at RT and processed for whole-mount in situ hybridization in the protocol previously described (Harland, 1991).

To count the number of cells in streams of different width, 3D confocal imaging was performed in TgSox10:nucRFP/mGFP zebrafish embryos as previously described (Moore et al., 2013) and in *Xenopus* embryos in which the NCCs were labeled by grafting NC expressing nuclear GFP (Theveneau et al., 2013).

### Confrontation and stripe assays

In vitro analysis of NC migration was performed using wild-type NC explants cultured on Fn alone or Fn and versican V0/V1 protein–coated plates. Versican V0/V1 protein coating was performed by incubating 50 × 9–mm plastic Petri dishes at 37°C with a versican/PBS solution at 0.7 µg/ml, mixed with fluorescein-dextran for 1 h, and washed with PBS. Once the dish was coated with versican, two separate assays were prepared. For the confrontational assay, half the versican coating was removed, and the plate was reincubated with 10 µg/ml Fn for 1 h and washed with PBS. For the stripe assay, versican was removed to create alternating stripes, and the plate was reincubated with 10 µg/ml Fn for 1 h and washed with PBS. In order generate a dorsal start point for NC migration, a horizontal line was etched onto the plate. Control dishes were done by incubating Fn and BSA alone. Once the NC had been dissected, it was transferred onto the Fn-coated area and allowed to attach for 30 min at RT before imagining.

### Time-lapse video microscopy

For time-lapse recordings, images were captured every 3–5 min for a total of 8 h using Plan Fluor 10×/0.30 DIC L/N1 objectives with DM5500 and DMRXA2 compound microscopes (Leica Biosystems) at 18°C with either a DFC 300FX camera (Leica Biosystems) and LAS acquisition software or an Orca-5G camera (Hamamatsu Photonics) and SimplePCI software. For in vivo imaging, embryos were immobilized onto plasticine. Time-lapse and NCC tracking was performed using the ImageJ Manual Tracking plug-in as previously described (Carmona-Fontaine et al., 2008; Matthews et al., 2008). Time-lapse imaging for CIL and CoA assays was performed at 18°C in Danilchick's medium using an upright microscope (Eclipse 80i; Nikon) fitted with an objective (Plan Fluor 10×/0.30 DIC L/N1) and a camera (ORCA-05G; Hamamatsu Photonics). Data were acquired using SimplePCI software. Confocal images were acquired at 22°C in Danilchick's medium using a TCS SPE upright microscope (Leica Biosystems) fitted with a HC PL APO 20×/0.75 IMM CS2 water objective. ISH images were captured at 18°C using a stereomicroscope (MZ FLIII; Leica Biosystems) fitted with a Plan 1.0×/0.125 objective and a camera (DFC420; Leica Biosystems). Data were acquired using IM50 v5 software (Leica Biosystems).

### Statistics

Normal distributions were described using the mean and either the standard error of the mean or SD as noted for bar graphs with error bars. Nonnormal data distributions were described using median, lower, and upper quartiles, and minimum and maximum values, and represented using bar-and-whisker graphs, where whiskers show minimum and maximum values, boxes indicate lower and upper percentile, and bars show the median value. Significance for differences was calculated with a two-sided Student's *t* test for normally distributed data or a two-sided two-sample Mann-Whitney *U* test for nonnormal data (***, $P < 0.001$; **, $P < 0.01$).

### Quantification of dispersion

Dispersion of simulated cell clusters was quantified using the Delaunay triangulation method (Carmona-Fontaine et al., 2011). In brief, the centroid position of the cells is used to create a Delaunay tessellation of the cell configuration. The resulting median of the triangle areas are compared at the end of the observation period and at the beginning of the observation period, and the ratio of these values is defined as the dispersion of the population.

### Persistence

Movement persistence of trajectories is calculated by measuring the maximum distance along the trajectory and dividing by the total length of the trajectory (Vedel et al., 2013).

### CPM of NC migration

Our model of NC migration is based on the CPM (Graner and Glazier, 1992) using the Tissue Simulation Toolkit implementation package (Merks and Glazier, 2005; https://sourceforge.net/projects/tst/). Cells are represented as domains on a 2D grid with an integer $\sigma(x)$ in every grid point $x$ denoting the ID of the cell occupying that grid point and $\sigma(x) = 0$ designating cell free areas (medium). The same grid is used to describe the concentration distribution of chemoattractant C3a as $c(x)$ at every point $x$. Each configuration $\xi$ is characterized by a scalar valued function, the Hamiltonian, as

$$H(\xi) = \sum_{i=1}^{N} \lambda_V \left[V(i) - V_T(i)\right]^2 + \sum_{\langle x,y \rangle} J_{x,y}\left[1 - \delta(x,y)\right].$$

The first sum runs through cells and characterizes the deviation of cell areas $V(i)$ from a target area $V_T(i)$ and is referred to as the volume term. The second term sums all cell borders with different weights $J_{x,y}$ assigned to different boundary types (e.g., cell–cell boundaries, cell–medium boundaries) and is referred to as the adhesion term. Function $\delta(x,y)$ is the Kronecker-delta function: $\delta(x,y) = 1$ if $x = y$, otherwise $\delta = 0$. Cell movement results from a series of attempts to update the cell IDs on the grid. In such an update attempt, a target site $b$ and one of its neighbors, $a$, are selected at random and an attempt is made to copy the source value $\sigma(a)$ to target site $b$. The probability of overwriting $\sigma(b)$ with $\sigma(a)$ is defined as $P[\sigma(a) \rightarrow b] = \min(1, \exp\{w[\sigma(a) \rightarrow b] - \Delta H[\sigma(a) \rightarrow b]\})$. Here, $\Delta H[\sigma(a) \rightarrow b]$ is the change in $H(\xi)$ caused by the copy attempt and $w[\sigma(a) \rightarrow b]$ is

$$w[\sigma(a) \rightarrow b] = \lambda_c[c(b) - c(a)] \cdot \delta[\sigma(a)] \cdot \{1 - \delta[\sigma(b)]\} + \lambda_p \sum_{i=[\sigma(a),\sigma(b)]} \frac{\Delta r_i p_i}{|p_i|} + \lambda_m \sum_{i=[\sigma(a),\sigma(b)]} \Delta r_i \cdot \sum_{j \in [n(i)]} \frac{r_{i,j}}{|r_{i,j}|} \cdot \left(|r_{i,j}| - d_0\right).$$

The first term describes cell expansion caused by chemotaxis at free cell boundaries with an affinity of $\lambda_c$ (Merks et al., 2008). Again, $\delta(i) = 1$ only if $i = 0$. The second term enhances cell displacements caused by the copy attempt ($\Delta r_i$) in the direction of the cell's internal polarization direction $p_i$ with relative strength $\lambda_p$ (Szabó et al., 2010). The third term describes the bias produced by an elastic mechanical link between cell $i$ and its linked neighbors $n(i)$, with $r_{i,j} = r_j - r_i$ (where $r_i$ is the position of cell $i$) and $d_0$ denoting the diameter of cells. Such links are established between touching cells with a probability of $p_+ = 0.1$ and are removed with probability $p_- = \min[1,(|r_{i,j}| - d_0)/100]$ and are responsible for adjusting the viscosity of the migrating cluster (Czirók et al., 2013; Kuriyama et al., 2014).

The usual time step in the CPM is the Monte Carlo step (MCS), defined as $N$ copy attempts, where $N$ is the number of grid points in the system. After each MCS the polarity vectors are updated with the cell displacement in that MCS ($\Delta R_i(t)$) as $p_i(t+1) = (1 - \delta_i)p_i(t) + \Delta R_i(t)$, where $\delta_i$ is the persistence decay coefficient of cell motion (Szabó et al., 2010), which depends on whether the cell is in contact with any other cell or not. Whenever two cells are in contact for at least $\Delta t$ time, the polarization vector of both cells is additionally updated to represent a repolarization bias away from the contact:

$$p_i^{CIL}(t+1) = p_i(t+1) - \lambda_r \frac{r_{i,j}}{|r_{i,j}|},$$

where $\lambda_r$ represents the strength of the repolarization.

To allow a more realistic cluster spreading, we consider inserting a cell-free area between cells during a copy attempt (Szabó et al., 2012) with a constant probability of 0.1. In this case, the chemotaxis term is set to zero and only the retracting cell is considered in the other terms. Additionally, when the elementary copy attempt would cause a cell to lose its connectivity (i.e., the cell would be split), an additional $\Delta H_{conn}$ penalty is added to the $\Delta H$ function to reduce the probability of accepting such a copy.

Chemoattractant secretion, diffusion, and decay are simulated using a forward Euler method to solve the discretized diffusion equation $\partial_t c(t,x) = D\nabla^2 c(t,x) + s_c \cdot \delta_{cell} - d_c \cdot c(t,x)$. Here, $D$ is the diffusion coefficient; secretion only occurs at positions that are occupied by a cell (expressed by the function $\delta_{\text{cell}} = 1$ (only at sites occupied by cells) at a rate $s_c$, whereas decay is described by a decay rate $d_c$. The diffusion equation is iterated sufficient number of times between each MCS to avoid numerical instabilities caused by high $D$. The effect of versican is implemented in the model as a stationary chemorepellent. At boundaries, versican is present as a linear gradient spanning a range of 50 µm (10 lattice sites).

### Model parameters

Cells with a target area of 25 grid points were initialized in a tightly packed cluster of 50 cells in a system of either 300 × 300 or 70 × 300 grid points to represent unconfined or confined geometries. In confined geometries, 25 grid points were added to the confinement width on both sides with 10 grid sites on both side reserved for the versican boundary. For large clusters, the simulation area was increased to accommodate a cell-free area at least 260 grid points in length from the edge of the cluster. Dorsal boundaries and strict confinement boundaries are nonpermissive, and copying onto a boundary site is not allowed for cells. Cell size calibrates our model to 1 grid point = 5 µm, and we chose 1 MCS = 15 s. Simulations are run for 2,400 MCS (10 h), with an additional 500 MCS initial annealing phase without cell propulsion to remove any bias from artificial cell shape initialization and build up a steady-state chemoattractant concentration field. Adhesion values are set to neutral ($J_{cell-cell} = 1$, $J_{cell-medium} = 0.5$), and the relative importance of the terms are set to $\lambda_V = 1$, $\lambda_c = 0.2$, $\lambda_p = 0.65$, $\lambda_m = 1.25$, and $\lambda_r = 0.05$, unless otherwise stated. Repolarization delay is set to $\Delta t = 8$ MCS to obtain a contact duration distribution (Fig. S3 B) that is compatible with experimental observations (Woods et al., 2014). The polarity decay parameter was set to $\delta_f = 0.3$ for free cells and $\delta_C = 0.06$ for cells in contact to achieve realistic persistence of free cells and cells in clusters (Fig. S3 A, Pc = 0.13, Pf = 0.5). Parameters for the diffusion

process were set to mimic the parameters of small diffusing molecules (Belle et al., 2006; Lin and Butcher, 2006) and to provide a characteristic diffusion length of ∼100 µm (Carmona-Fontaine et al., 2011; Woods et al., 2014): $D = 8$, $d_c = 0.006$, and secretion is set to $s_c = 10$. Absorbing boundaries are set for the diffusion process ($c = 0$), which are also extended for an additional 100 grid points from the cell arena to allow a smooth diffusion field and to avoid mayor boundary effects.

### DEM model of NC migration

In the following, we describe the DEM model of NC migration used for this study, which is based on the model described and analyzed previously (Woods et al., 2014). Cells in this 2D model are represented as point particles with a position and velocity and a finite contact radius R. If the centers of two cells are within 2R distance, they are considered to be in contact. Cell motion is governed through a secondary dynamics, which is integrated using a forward Euler method. For cell $i$:

$$\begin{aligned} v_i(t+1) &= v_i(t) + \frac{f_i(t)}{m}\Delta t \\ r_i(t+1) &= r_i(t) + v_i(t)\Delta t, \end{aligned}$$

where $v_i(t)$, $r_i(t)$, and $f_i(t)$ are the velocity, position, and forces acting on cell $i$ at time $t$, $\Delta t$ is the integration time step, and $m$ is the mass of the cell. The forces acting on the cell depend on the state of the cell, in particular whether it is in contact with other cells or not (free).

Forces acting on free cells ensure that it is attracted to other cells (CoA), it periodically tumbles by abruptly changing its migration direction and maintains an approximately constant speed:

$$f_i^F(t) = \kappa_C \cdot m\alpha_C |v_i(t)| \nabla \varphi_i(t) + \kappa_T \frac{m}{\Delta t}\left[|v_i(t)| n_\omega - v_i(t)\right] + \kappa_S m \alpha_p \left[S\hat{v}_i(t) - v_i(t)\right].$$

The first term describes CoA, where $\nabla \varphi_i(t)$ represents the gradient of a field of chemoattractant that is diffusing from cells and decaying and is assumed to have reached a steady state. Therefore, the chemoattractant level sensed by cell $i$ is

$$\varphi_i(t) = \sum_j c_0 \exp\left[-H\left(r_j - R_i\right)\right],$$

where $R_i = r_i + R_s v_i(t)$ is the position of chemoattractant sensing of cell $i$ with $R_s = 18\ \mu m$, and $H$ is a parameter constant related to the diffusion length of the chemoattractant molecule. Concentration levels are measured in arbitrary units; therefore, we chose $c_0 = 1$. The function $\kappa_C(t)$ is constructed such that it ensures that CoA acts only once every 2 s on the cell. The second term in the equation of the force describes tumbling. Here, the function $\kappa_T(t)$ is constructed such that it ensures that the cell tumbles once every 5 min. During tumbling, the cell's direction of motion is forced to turn in a randomly chosen $n_\omega$ direction. Finally, the last term forces the cell to assume speed $S$. $\hat{v}_i(t)$ is the unit-vector pointing in the direction of $v_i(t)$.

Forces acting on cells that are in contact are

$$f_i^C(t) = \sum_j \left\{-K\delta_{ij}^{3/2}(t) - D\sqrt{mK}\cdot\delta_{ij}^{1/4}(t)\cdot V_{ij}(t) + \kappa_R(ij) m \alpha_R \left[S n_{CIL} - v_i(t)\right]\right\}.$$

The summation runs over all cells other than $i$. The first term describes an elastic contact force, with $K$ being the effective stiffness parameter of the cells and $\delta_{ij}$ being the overlap between the two cells ($\delta_{ij} = 2R - |r_i - r_j|$). The second term describes a dissipative contact force, with $V_{ij}(t)$ being the relative velocity of the two cells: $V_{ij}(t) = \{(v_i(t) - v_j(t))\, n_{ij}(t)\}\ n_{ij}(t)$, where $n_{ij}(t)$ is the unit vector pointing from cell i to cell j. Parameter $D$ describes the effect of contact dampening. The last term describes CIL. The function $\kappa_R(ij)$ is a Heaviside step function with zero value until the cells $i$ and $j$ have been in continuous contact for 10 min, and it is one after that. The CIL force acts to turn the velocity vector in the direction of $n_{CIL}$, which is chosen randomly from the interval $[n_{ij}(t) + 0.5\pi: n_{ij}(t) + 1.5\,\pi]$.

Lateral boundaries are represented as a constant force field acting on cells that enter the boundary region with a strength $f_B$. As in the CPM implementation, the boundary region is restricted to 50 µm on either side of the corridor. The dorsal boundary is implemented by constructing a virtual mirror cell on the opposite side of the dorsal boundary that acts on the approaching real cell and consequently prevents the real cell to cross the dorsal border.

Parameters are based on the previous study (Woods et al., 2014): $S = 4 \times 10^{-8}$, $\alpha_p = 1$, $\alpha_R = 0.003$, $\alpha_c = 1.5\text{e}3$, $f_B = 10^{-8}$, $H = 6301.338$, $m = 10^{-10}$, $R = 20$ µm, $K = 0.1124365$, $D = 2.199$, and $\Delta t = 1$ ms. Simulation arena size was chosen to be $L_x = 1{,}800$ µm and $L_y = 1{,}000$ µm for unconstrained simulations and $L_x = 220$ µm and $L_y = 1{,}000$ µm for constrained simulations. A total of 50 cells were initialized in five columns and 10 rows.

### Online supplemental material

Fig. S1 shows the expression levels of versican isoforms at various developmental stages and the placodal ectoderm and the pharyngeal endoderm tissues adjacent to the NC. Fig. S2 shows the specificity of the VsMO injections, the effect of VsMO at the later stage 25, CIL and CoA unaffected by VsMO, a rescue experiment using versican-soaked microbeads, quantification of the graft experiments in Fig. 2 (F and G), the effect of VsMO on placode organization, melanocyte numbers, and cartilage formation. Fig. S3 provides further information on the computational model behavior. Videos 1 and 2 show simulations of CPM and DEM models of NC migration with and without confinement. Video 3 contains time-lapse recordings of in vivo grafted NCC and is related to Fig. 4 (A and C). Video 4 shows NC explants plated in scratch assay or on fibronectin and is related to Fig. 4 (L and N). Video 5 shows simulations with varying confinement widths and cell numbers and is related to Fig. 5 B. Online supplemental material is available http://www.jcb.org/cgi/content/full/jcb.201602083/DC1.


## Acknowledgments

We thank Claudia Linker for comments on the manuscript.

This study was supported by grants from Medical Research Council (M010465 and J000655) and Biotechnology and Biological Sciences Research Council (M008517) and Wellcome Trust to R. Mayor and by a Marie Curie Fellowship (329968) to A. Szabó. The authors acknowledge the use of the University College London Legion High Performance Computing Facility, and associated support services, in the completion of this work.

The authors declare no competing financial interests.

Submitted: 25 February 2016
Accepted: 12 May 2016


## References


Alfandari, D., H. Cousin, A. Gaultier, B.G. Hoffstrom, and D.W. DeSimone. 2003. Integrin α5β1 supports the migration of *Xenopus* cranial neural crest on fibronectin. *Dev. Biol.* 260:449–464. http://dx.doi.org/10.1016/S0012-1606(03)00277-X

Baker, R.K., and P.B. Antin. 2003. Ephs and ephrins during early stages of chick embryogenesis. *Dev. Dyn.* 228:128–142. http://dx.doi.org/10.1002/dvdy.10354

Beck, C.W., and J.M. Slack. 1999. A developmental pathway controlling outgrowth of the *Xenopus* tail bud. *Development.* 126:1611–1620.

Belle, A., A. Tanay, L. Bitincka, R. Shamir, and E.K. O'Shea. 2006. Quantification of protein half-lives in the budding yeast proteome. *Proc. Natl. Acad. Sci. USA.* 103:13004–13009. http://dx.doi.org/10.1073/pnas.0605420103

Beltman, J.B., A.F.M. Marée, J.N. Lynch, M.J. Miller, and R.J. de Boer. 2007. Lymph node topology dictates T cell migration behavior. *J. Exp. Med.* 204:771–780. http://dx.doi.org/10.1084/jem.20061278

Carmona-Fontaine, C., H.K. Matthews, S. Kuriyama, M. Moreno, G.A. Dunn, M. Parsons, C.D. Stern, and R. Mayor. 2008. Contact inhibition of locomotion in vivo controls neural crest directional migration. *Nature.* 456:957–961. http://dx.doi.org/10.1038/nature07441

Carmona-Fontaine, C., E. Theveneau, A. Tzekou, M. Tada, M. Woods, K.M. Page, M. Parsons, J.D. Lambris, and R. Mayor. 2011. Complement fragment C3a controls mutual cell attraction during collective cell migration. *Dev. Cell.* 21:1026–1037. http://dx.doi.org/10.1016/j.devcel.2011.10.012

Casini, P., M. Ori, A. Avenoso, A. D'Ascola, P. Traina, W. Mattina, R. Perris, G.M. Campo, A. Calatroni, I. Nardi, and S. Campo. 2008. Identification and gene expression of versican during early development of *Xenopus*. *Int. J. Dev. Biol.* 52:993–998. http://dx.doi.org/10.1387/ijdb.082582pc

Czirók, A., K. Varga, E. Méhes, and A. Szabó. 2013. Collective cell streams in epithelial monolayers depend on cell adhesion. *New J. Phys.* 15:075006. http://dx.doi.org/10.1088/1367-2630/15/7/075006

David, R., K. Ahrens, D. Wedlich, and G. Schlosser. 2001. Xenopus Eya1 demarcates all neurogenic placodes as well as migrating hypaxial muscle precursors. *Mech. Dev.* 103:189–192. http://dx.doi.org/10.1016/S0925-4773(01)00355-0

De Bellard, M.E., Y. Rao, and M. Bronner-Fraser. 2003. Dual function of Slit2 in repulsion and enhanced migration of trunk, but not vagal, neural crest cells. *J. Cell Biol.* 162:269–279. http://dx.doi.org/10.1083/jcb.200301041

De Calisto, J., C. Araya, L. Marchant, C.F. Riaz, and R. Mayor. 2005. Essential role of non-canonical Wnt signalling in neural crest migration. *Development.* 132:2587–2597. http://dx.doi.org/10.1242/dev.01857

DeSimone, D.W., L.A. Davidson, M. Marsden, and D. Alfandari. 2005. The *Xenopus* embryo as a model system for studies of cell migration. *In* Cell Migration. Humana Press, Totowa, NJ. 235–246.

Donà, E., J.D. Barry, G. Valentin, C. Quirin, A. Khmelinskii, A. Kunze, S. Durdu, L.R. Newton, A. Fernandez-Minan, W. Huber, et al.. 2013. Directional tissue migration through a self-generated chemokine gradient. *Nature.* 503:285–289. http://dx.doi.org/10.1038/nature12635

Doxzen, K., S.R.K. Vedula, M.C. Leong, H. Hirata, N.S. Gov, A.J. Kabla, B. Ladoux, and C.T. Lim. 2013. Guidance of collective cell migration by substrate geometry. *Integr Biol (Camb).* 5:1026–1035. http://dx.doi.org/10.1039/c3ib40054a

Dutt, S., M. Kléber, M. Matasci, L. Sommer, and D.R. Zimmermann. 2006. Versican V0 and V1 guide migratory neural crest cells. *J. Biol. Chem.* 281:12123–12131. http://dx.doi.org/10.1074/jbc.M510834200

Dutt, S., E. Cassoly, M.T. Dours-Zimmermann, M. Matasci, E.T. Stoeckli, and D.R. Zimmermann. 2011. Versican V0 and V1 direct the growth of peripheral axons in the developing chick hindlimb. *J. Neurosci.* 31:5262–5270. http://dx.doi.org/10.1523/JNEUROSCI.4897-10.2011

Erickson, C.A. 1985. Control of neural crest cell dispersion in the trunk of the avian embryo. *Dev. Biol.* 111:138–157. http://dx.doi.org/10.1016/0012-1606(85)90442-7

Graner, F., and J.A. Glazier. 1992. Simulation of biological cell sorting using a two-dimensional extended Potts model. *Phys. Rev. Lett.* 69:2013–2016. http://dx.doi.org/10.1103/PhysRevLett.69.2013

Harland, R.M. 1991. *Xenopus laevis*: practical uses in cell and molecular biology. 36. Elsevier. 685-95 pp.

Henderson, D.J., P. Ybot-Gonzalez, and A.J. Copp. 1997. Over-expression of the chondroitin sulphate proteoglycan versican is associated with defective neural crest migration in the Pax3 mutant mouse (splotch). *Mech. Dev.* 69:39–51. http://dx.doi.org/10.1016/S0925-4773(97)00151-2

Hopwood, N.D., A. Pluck, and J.B. Gurdon. 1989. A *Xenopus* mRNA related to *Drosophila* twist is expressed in response to induction in the mesoderm and the neural crest. *Cell.* 59:893–903. http://dx.doi.org/10.1016/0092-8674(89)90612-0

Jia, L., L. Cheng, and J. Raper. 2005. Slit/Robo signaling is necessary to confine early neural crest cells to the ventral migratory pathway in the trunk. *Dev. Biol.* 282:411–421. http://dx.doi.org/10.1016/j.ydbio.2005.03.021

Jorn, S., F. Peruani, and A. Deutsch. 2007. Bacterial swarming driven by rod shape. *In* Mathematical Modeling of Biological Systems, Volume I. Birkhauser, Boston, MA. 163–174.

Kawasaki, T., Y. Bekku, F. Suto, T. Kitsukawa, M. Taniguchi, I. Nagatsu, T. Nagatsu, K. Itoh, T. Yagi, and H. Fujisawa. 2002. Requirement of neuropilin 1-mediated Sema3A signals in patterning of the sympathetic nervous system. *Development.* 129:671–680.

Kerr, R.S., and D.F. Newgreen. 1997. Isolation and characterization of chondroitin sulfate proteoglycans from embryonic quail that influence neural crest cell behavior. *Dev. Biol.* 192:108–124. http://dx.doi.org/10.1006/dbio.1997.8731

Kulesa, P.M., and S.E. Fraser. 1998. Neural crest cell dynamics revealed by time-lapse video microscopy of whole embryo chick explant cultures. *Dev. Biol.* 204:327–344. http://dx.doi.org/10.1006/dbio.1998.9082

Kulesa, P., M. Bronner-Fraser, and S. Fraser. 2000. In ovo time-lapse analysis after dorsal neural tube ablation shows rerouting of chick hindbrain neural crest. *Development.* 127:2843–2852.

Kuriyama, S., E. Theveneau, A. Benedetto, M. Parsons, M. Tanaka, G. Charras, A. Kabla, and R. Mayor. 2014. In vivo collective cell migration requires an LPAR2-dependent increase in tissue fluidity. *J. Cell Biol.* 206:113–127. http://dx.doi.org/10.1083/jcb.201402093

Landolt, R.M., L. Vaughan, K.H. Winterhalter, and D.R. Zimmermann. 1995. Versican is selectively expressed in embryonic tissues that act as barriers to neural crest cell migration and axon outgrowth. *Development.* 121:2303–2312.

Leong, M.C., S.R.K. Vedula, C.T. Lim, and B. Ladoux. 2013. Geometrical constraints and physical crowding direct collective migration of fibroblasts. *Commun. Integr. Biol.* 6:e23197. http://dx.doi.org/10.4161/cib.23197

Lin, F., and E.C. Butcher. 2006. T cell chemotaxis in a simple microfluidic device. *Lab Chip.* 6:1462–1469. http://dx.doi.org/10.1039/B607071J

Londono, C., M.J. Loureiro, B. Slater, P.B. Lücker, J. Soleas, S. Sathananthan, J.S. Aitchison, A.J. Kabla, and A.P. McGuigan. 2014. Nonautonomous contact guidance signaling during collective cell migration. *Proc. Natl. Acad. Sci. USA.* 111:1807–1812. http://dx.doi.org/10.1073/pnas.1321852111

Marée, A.F., A.V. Panfilov, and P. Hogeweg. 1999. Migration and thermotaxis of *Dictyostelium discoideum* slugs, a model study. *J. Theor. Biol.* 199:297–309. http://dx.doi.org/10.1006/jtbi.1999.0958

Marel, A.-K., M. Zorn, C. Klingner, R. Wedlich-Söldner, E. Frey, and J.O. Rädler. 2014. Flow and diffusion in channel-guided cell migration. *Biophys. J.* 107:1054–1064. http://dx.doi.org/10.1016/j.bpj.2014.07.017

Matthews, H.K., L. Marchant, C. Carmona-Fontaine, S. Kuriyama, J. Larraín, M.R. Holt, M. Parsons, and R. Mayor. 2008. Directional migration of neural crest cells in vivo is regulated by Syndecan-4/Rac1 and non-canonical Wnt signaling/RhoA. *Development.* 135:1771–1780. http://dx.doi.org/10.1242/dev.017350

Mayor, R., R. Morgan, and M.G. Sargent. 1995. Induction of the prospective neural crest of *Xenopus*. *Development.* 121:767–777.

McLennan, R., J.M. Teddy, J.C. Kasemeier-Kulesa, M.H. Romine, and P.M. Kulesa. 2010. Vascular endothelial growth factor (VEGF) regulates cranial neural crest migration in vivo. *Dev. Biol.* 339:114–125. http://dx.doi.org/10.1016/j.ydbio.2009.12.022

Mellott, D.O., and R.D. Burke. 2008. Divergent roles for Eph and ephrin in avian cranial neural crest. *BMC Dev. Biol.* 8:56. http://dx.doi.org/10.1186/1471-213X-8-56

Merks, R.M.H., and J.A. Glazier. 2005. A cell-centered approach to developmental biology. *Physica A.* 352:113–130. http://dx.doi.org/10.1016/j.physa.2004.12.028

Merks, R.M.H., S.V. Brodsky, M.S. Goligorksy, S.A. Newman, and J.A. Glazier. 2006. Cell elongation is key to in silico replication of in vitro vasculogenesis and subsequent remodeling. *Dev. Biol.* 289:44–54. http://dx.doi.org/10.1016/j.ydbio.2005.10.003

Merks, R.M.H., E.D. Perryn, A. Shirinifard, and J.A. Glazier. 2008. Contact-inhibited chemotaxis in de novo and sprouting blood-vessel growth. *PLOS Comput. Biol.* 4:e1000163. (published erratum appears in *PLoS Comput Biol.* 2015]) http://dx.doi.org/10.1371/journal.pcbi.1000163

Mjaatvedt, C.H., H. Yamamura, A.A. Capehart, D. Turner, and R.R. Markwald. 1998. The Cspg2 gene, disrupted in the hdf mutant, is required for right cardiac chamber and endocardial cushion formation. *Dev. Biol.* 202:56–66. http://dx.doi.org/10.1006/dbio.1998.9001

Moore, R., E. Theveneau, S. Pozzi, P. Alexandre, J. Richardson, A. Merks, M. Parsons, J. Kashef, C. Linker, and R. Mayor. 2013. Par3 controls neural crest migration by promoting microtubule catastrophe during contact inhibition of locomotion. *Development.* 140:4763–4775. http://dx.doi.org/10.1242/dev.098509

Newgreen, D.F., I.L. Gibbins, J. Sauter, B. Wallenfels, and R. Wütz. 1982. Ultrastructural and tissue-culture studies on the role of fibronectin, collagen and glycosaminoglycans in the migration of neural crest cells in the fowl embryo. *Cell Tissue Res.* 221:521–549. http://dx.doi.org/10.1007/BF00215700

Nieuwkoop, P., and J. Faber. 1967. Normal Table of *Xenopus laevis*: A Systematical and Chronological Survey of the Development from the

Fertilized Egg till the End of Metamorphosis. North Holland Publishing Co, Amsterdam. 260 pp.

Perissinotto, D., P. Iacopetti, I. Bellina, R. Doliana, A. Colombatti, Z. Pettway, M. Bronner-Fraser, T. Shinomura, K. Kimata, M. Mörgelin, et al. 2000. Avian neural crest cell migration is diversely regulated by the two major hyaluronan-binding proteoglycans PG-M/versican and aggrecan. *Development.* 127:2823–2842.

Perris, R., and S. Johansson. 1987. Amphibian neural crest cell migration on purified extracellular matrix components: a chondroitin sulfate proteoglycan inhibits locomotion on fibronectin substrates. *J. Cell Biol.* 105:2511–2521. http://dx.doi.org/10.1083/jcb.105.6.2511

Perris, R., and S. Johansson. 1990. Inhibition of neural crest cell migration by aggregating chondroitin sulfate proteoglycans is mediated by their hyaluronan-binding region. *Dev. Biol.* 137:1–12. http://dx.doi.org/10.1016/0012-1606(90)90002-Z

Perris, R., and D. Perissinotto. 2000. Role of the extracellular matrix during neural crest cell migration. *Mech. Dev.* 95:3–21. http://dx.doi.org/10.1016/S0925-4773(00)00365-8

Perris, R., J. Löfberg, C. Fällström, Y. von Boxberg, L. Olsson, and D.F. Newgreen. 1990. Structural and compositional divergencies in the extracellular matrix encountered by neural crest cells in the white mutant axolotl embryo. *Development.* 109:533–551.

Perris, R., D. Krotoski, T. Lallier, C. Domingo, J.M. Sorrell, and M. Bronner-Fraser. 1991. Spatial and temporal changes in the distribution of proteoglycans during avian neural crest development. *Development.* 111:583–599.

Perris, R., D. Perissinotto, Z. Pettway, M. Bronner-Fraser, M. Mörgelin, and K. Kimata. 1996. Inhibitory effects of PG-H/aggrecan and PG-M/versican on avian neural crest cell migration. *FASEB J.* 10:293–301.

Pettway, Z., M. Domowicz, N.B. Schwartz, and M. Bronner-Fraser. 1996. Age-dependent inhibition of neural crest migration by the notochord correlates with alterations in the S103L chondroitin sulfate proteoglycan. *Exp. Cell Res.* 225:195–206. http://dx.doi.org/10.1006/excr.1996.0170

Pohl, B.S., S. Knöchel, K. Dillinger, and W. Knöchel. 2002. Sequence and expression of FoxB2 (XFD-5) and FoxI1c (XFD-10) in *Xenopus* embryogenesis. *Mech. Dev.* 117:283–287. http://dx.doi.org/10.1016/S0925-4773(02)00184-3

Roffers-Agarwal, J., and L.S. Gammill. 2009. Neuropilin receptors guide distinct phases of sensory and motor neuronal segmentation. *Development.* 136:1879–1888. http://dx.doi.org/10.1242/dev.032920

Rubenstein, B.M., and L.J. Kaufman. 2008. The role of extracellular matrix in glioma invasion: a cellular Potts model approach. *Biophys. J.* 95:5661–5680. http://dx.doi.org/10.1529/biophysj.108.140624

Schwarz, Q., C.H. Maden, J.M. Vieira, and C. Ruhrberg. 2009. Neuropilin 1 signaling guides neural crest cells to coordinate pathway choice with cell specification. *Proc. Natl. Acad. Sci. USA.* 106:6164–6169. http://dx.doi.org/10.1073/pnas.0811521106

Shirinifard, A., J.S. Gens, B.L. Zaitlen, N.J. Popławski, M. Swat, and J.A. Glazier. 2009. 3D multi-cell simulation of tumor growth and angiogenesis. *PLoS One.* 4:e7190. http://dx.doi.org/10.1371/journal.pone.0007190

Stigson, M., J. Löfberg, and L. Kjellén. 1997. PG-M/versican-like proteoglycans are components of large disulfide-stabilized complexes in the axolotl embryo. *J. Biol. Chem.* 272:3246–3253. http://dx.doi.org/10.1074/jbc.272.6.3246

Szabó, A., and R. Mayor. 2016. Modelling collective cell migration of neural crest. *Curr. Opin. Cell Biol.* 42:22–28. http://dx.doi.org/10.1016/j.ceb.2016.03.023

Szabó, A., and R.M.H. Merks. 2013. Cellular potts modeling of tumor growth, tumor invasion, and tumor evolution. *Front. Oncol.* 3:87. http://dx.doi.org/10.3389/fonc.2013.00087

Szabó, A., E. Mehes, E. Kosa, and A. Czirók. 2008. Multicellular sprouting in vitro. *Biophys. J.* 95:2702–2710. http://dx.doi.org/10.1529/biophysj.108.129668

Szabó, A., R. Ünnep, E. Méhes, W.O. Twal, W.S. Argraves, Y. Cao, and A. Czirók. 2010. Collective cell motion in endothelial monolayers. *Phys. Biol.* 7:046007. http://dx.doi.org/10.1088/1478-3975/7/4/046007

Szabó, A., K. Varga, T. Garay, B. Hegedűs, and A. Czirók. 2012. Invasion from a cell aggregate--the roles of active cell motion and mechanical equilibrium. *Phys. Biol.* 9:016010. http://dx.doi.org/10.1088/1478-3975/9/1/016010

Theveneau, E., and R. Mayor. 2012. Neural crest delamination and migration: from epithelium-to-mesenchyme transition to collective cell migration. *Dev. Biol.* 366:34–54. http://dx.doi.org/10.1016/j.ydbio.2011.12.041

Theveneau, E., L. Marchant, S. Kuriyama, M. Gull, B. Moepps, M. Parsons, and R. Mayor. 2010. Collective chemotaxis requires contact-dependent cell polarity. *Dev. Cell.* 19:39–53. http://dx.doi.org/10.1016/j.devcel.2010.06.012

Theveneau, E., B. Steventon, E. Scarpa, S. Garcia, X. Trepat, A. Streit, and R. Mayor. 2013. Chase-and-run between adjacent cell populations promotes directional collective migration. *Nat. Cell Biol.* 15:763–772. http://dx.doi.org/10.1038/ncb2772

Turner, S., and J.A. Sherratt. 2002. Intercellular adhesion and cancer invasion: a discrete simulation using the extended Potts model. *J. Theor. Biol.* 216:85–100. http://dx.doi.org/10.1006/jtbi.2001.2522

Vedel, S., S. Tay, D.M. Johnston, H. Bruus, and S.R. Quake. 2013. Migration of cells in a social context. *Proc. Natl. Acad. Sci. USA.* 110:129–134. http://dx.doi.org/10.1073/pnas.1204291110

Vedula, S.R.K., M.C. Leong, T.L. Lai, P. Hersen, A.J. Kabla, C.T. Lim, and B. Ladoux. 2012. Emerging modes of collective cell migration induced by geometrical constraints. *Proc. Natl. Acad. Sci. USA.* 109:12974–12979. http://dx.doi.org/10.1073/pnas.1119313109

Vroomans, R.M.A., A.F.M. Marée, R.J. de Boer, and J.B. Beltman. 2012. Chemotactic migration of T cells towards dendritic cells promotes the detection of rare antigens. *PLOS Comput. Biol.* 8:e1002763. http://dx.doi.org/10.1371/journal.pcbi.1002763

Williams, D.R. Jr., A.R. Presar, A.T. Richmond, C.H. Mjaatvedt, S. Hoffman, and A.A. Capehart. 2005. Limb chondrogenesis is compromised in the versican deficient hdf mouse. *Biochem. Biophys. Res. Commun.* 334:960–966. http://dx.doi.org/10.1016/j.bbrc.2005.06.189

Woods, M.L., C. Carmona-Fontaine, C.P. Barnes, I.D. Couzin, R. Mayor, and K.M. Page. 2014. Directional collective cell migration emerges as a property of cell interactions. *PLoS One.* 9:e104969. http://dx.doi.org/10.1371/journal.pone.0104969